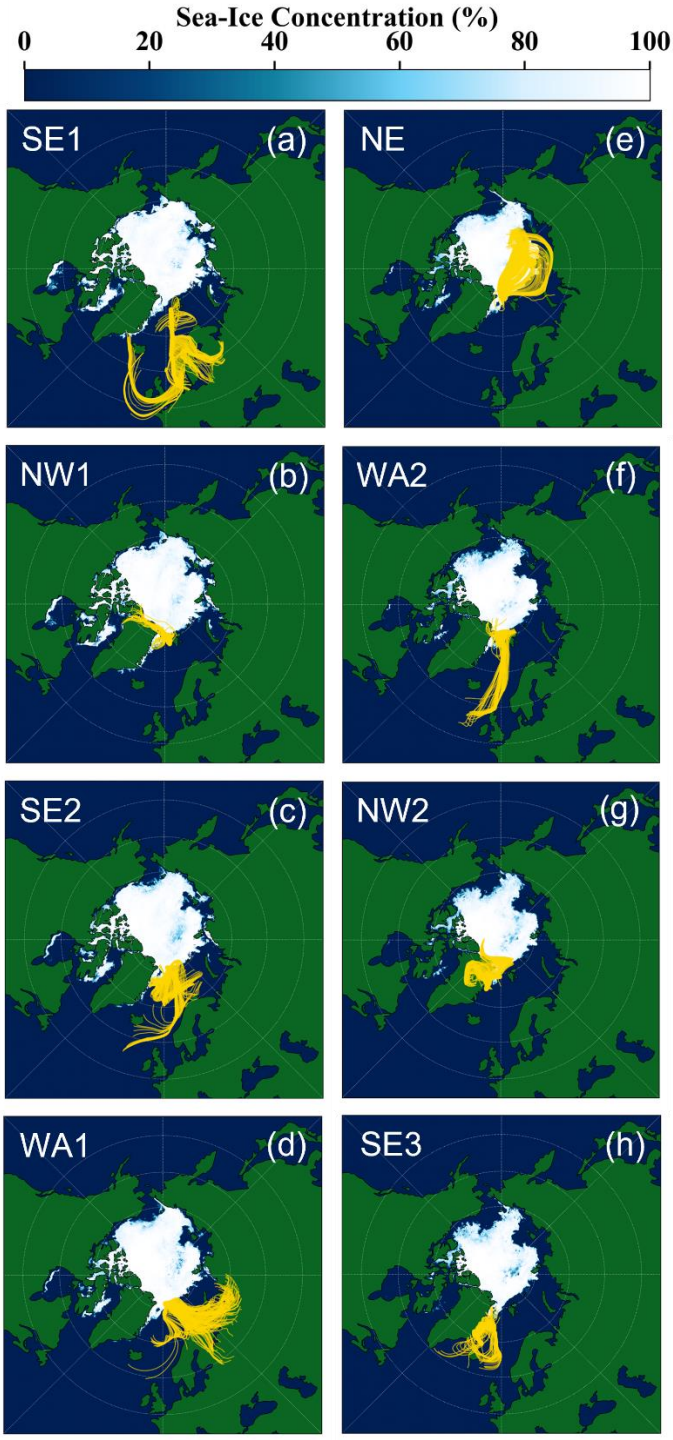


Figure S1: Backward airmass trajectories arriving at the ship position during the campaign segregated into different continuous airmass regimes ((a) SE1- South easterly 1, (b) NW1- North westerly 1, (c) SE2- South easterly 2, (d) WA1- Warm airmass intrusion 1, (e) NE- North easterly, (f) WA2- Warm airmass intrusion 2, (g) NW2- North westerly 2, (h) SE3- South easterly 3) during the study period. Sea ice concentrations indicate the condition during the time when the respective regimes were prevailing.

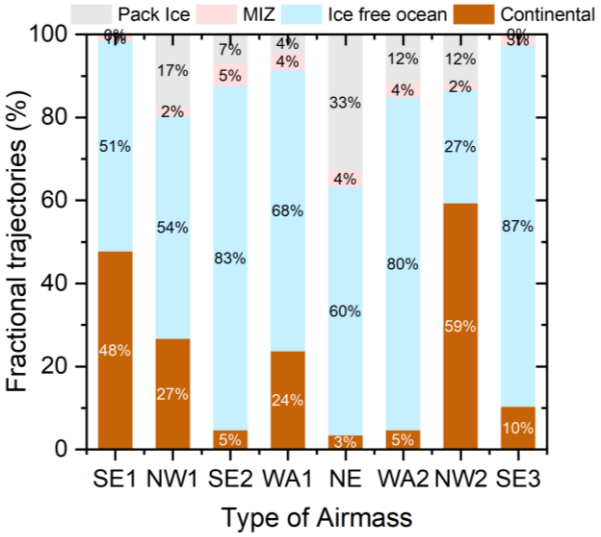


Figure S2: Stacked bar plots showing the fractional contributions of different surface types traversed by five-day airmass back trajectories arriving at the ship position, grouped into eight designated airmass sectors (see Fig. S1).

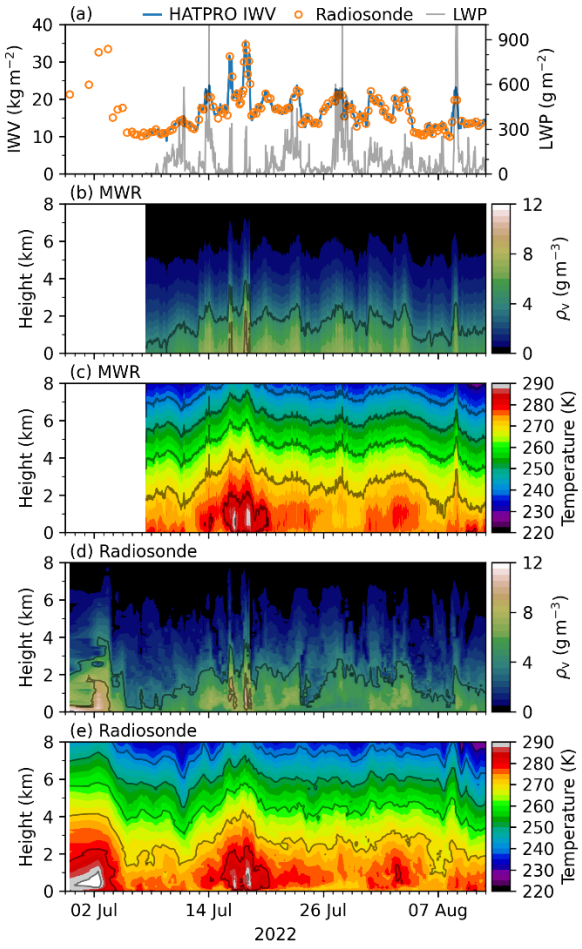


Figure S3: From top to bottom: (a) Integrated water vapor from HATPRO and Radiosonde observations (left y-axis), liquid water path (in gm^{-2}, right y-axis) (b) water vapor density from HATPRO radiometer (c) HATPRO microwave-radiometer retrieval of air temperature (K) vertical profiles, (d) water vapor density from Radiosondes, (e) vertical distribution of air temperature (K) from Radiosondes.

To characterize water vapor, cloud liquid, and boundary layer (BL) structure along the RV *Polarstern* track from the Fram Strait into the central Arctic and back, we combined continuous microwave radiometer profiling with a dense radiosonde program. The primary profiler was an RPG-HATPRO (Humidity and Temperature PROfiler). HATPRO measured upwelling brightness temperatures (BTs) in two bands: seven K-band channels (22-31 GHz) near the water-vapor absorption line and seven V-band channels (51-58 GHz). Zenith-staring radiometry provided near-continuous time series (~1 s sampling) from which we retrieved integrated water vapor (IWV), liquid water path (LWP), and coarse vertical profiles of absolute humidity and temperature using established retrievals. To better resolve the lowest kilometre, the instrument executed a boundary layer scan every 30 min (zenith + five low elevation angles), which increases sensitivity to near-surface temperature gradients and shallow inversions. The radiometer was calibrated regularly throughout the campaign (instrument tip curve and load checks as per manufacturer procedures), ensuring stable BT baselines across synoptic transitions. Routine 12 UTC soundings (DWD) provided the backbone of high-resolution vertical context and an independent evaluation of the radiometer retrievals. More details about these measurements and warm airmass intrusions are provided in Arun et al. (2026) and Kanzow et al. (2023).

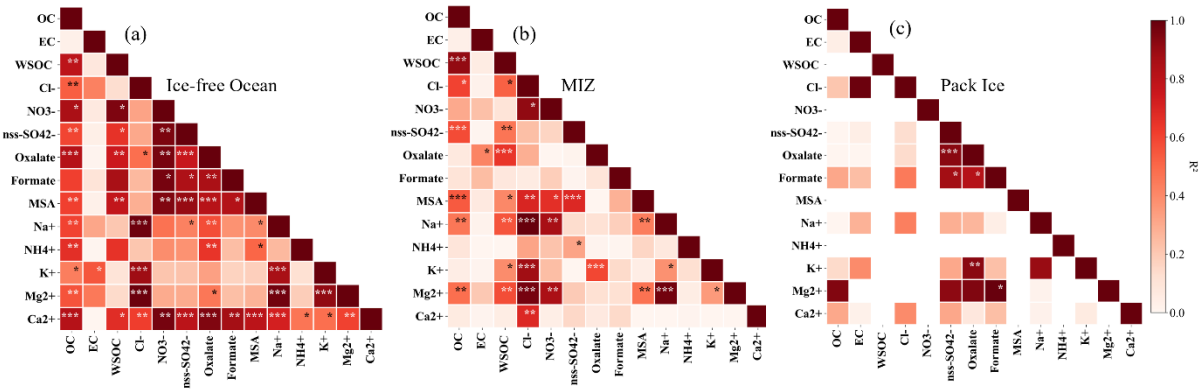
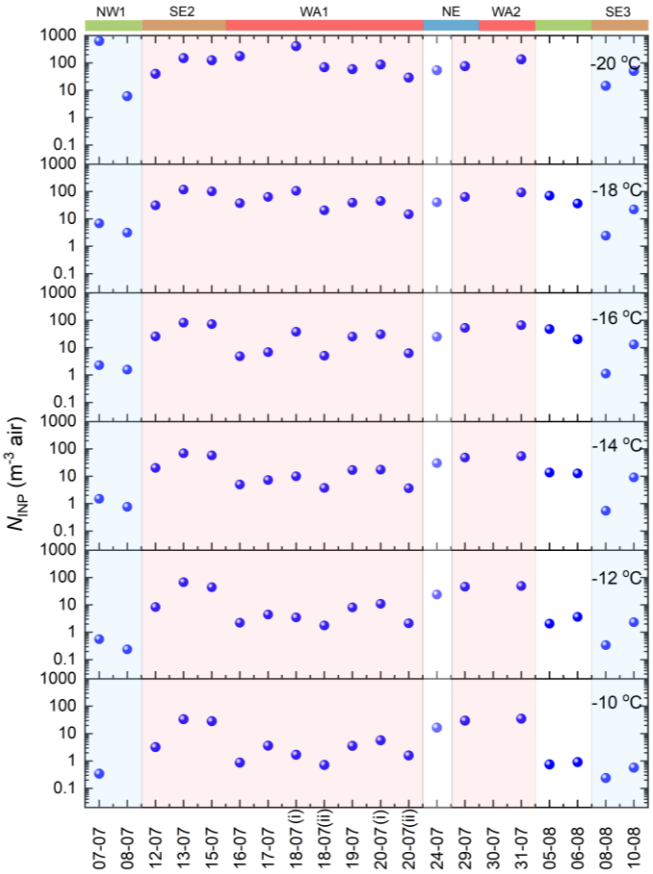
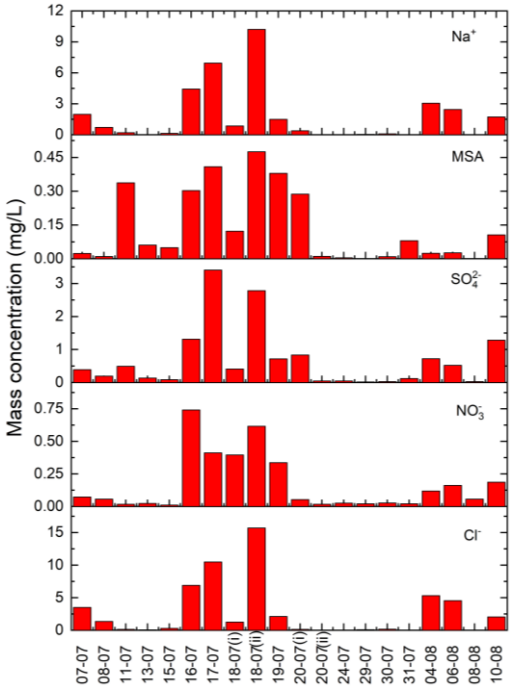


Figure-S4: Correlation between different chemical components measured in the aerosol filter samples collected over the (a) open ocean (n=12), (b) marginal ice zone (n=19), and (c) ice pack environments (n=8). Color shading represents the coefficient of determination (R^2), with blue indicating weak correlations and red indicating strong correlations. (Asterisks within each grid cell denotes significance: * = p<0.05, ** = p<0.01, and *** = p<0.001 respectively).



43

44 **Figure-S5:** Temporal evolution of atmospheric N_{INP} at selected activation temperatures derived from filter
45 samples collected from the bow crane analysed with LINA and INDA. For those samples collected on the same
46 day are marked as (i) and (ii) respectively. Background shading marks the environment encountered by the vessel
47 during each sample: blue=open ocean; red=marginal ice zone; white= pack ice.



48

49 **Figure-S6:** Major water-soluble ions evaluated from the atmospheric INP filter samples during the study. For
50 those samples collected on the same day are marked as (i) and (ii) respectively.

Table S1: Mass concentration of different chemical species measured during ATWAICE

Species	Environment (mean ± SD, units in ng m^{-3})		
	Open ocean	MIZ	Pack Ice
OC	290 ± 123	361.3 ± 191.8	232 ± 97
WSOC	85.9 ± 79.4	168 ± 162	32.3 ± 59.9
SO_4^{2-}	409 ± 346	388 ± 314	111 ± 82
NO_3^-	36.6 ± 61	44.3 ± 78.1	3
Cl^-	1133 ± 1087	531.8 ± 1136	18.3 ± 21.1
$C_2O_4^{2-}$	16.7 ± 17.2	30.1 ± 27	11.6 ± 8.7
Formate	6.2 ± 6.7	10.4 ± 13.9	31.3 ± 78.5
MSA^-	61.5 ± 96.8	80.5 ± 63	7.3 ± 11.1
Na^+	708 ± 677	374.8 ± 730	19.4 ± 22.9
NH_4^+	24.5 ± 22.2	55.1 ± 47.6	8.3 ± 11.6
K^+	12.9 ± 10.6	13.8 ± 19.9	4.9 ± 2.4
Mg^{2+}	57.7 ± 62	41.7 ± 73.8	7.4 ± 10.3
Ca^{2+}	63.9 ± 99.1	108.9 ± 232.8	14.5 ± 10.9

Table S2: Mass concentration of different chemical species measured in the fog water

Species	Environment (units in mg L^{-1})		
	Open ocean	MIZ	Pack Ice
DOC	28.4 ± 33.4	10.6 ± 6.2	8.5 ± 4.1
SO_4^{2-}	15.4 ± 8.4	3.8 ± 2.5	3.3 ± 1.7
NO_3^-	1.4 ± 1.4	0.64 ± 0.45	0.8 ± 0.5
Cl^-	77.4 ± 83.1	7.4 ± 11.9	7.6 ± 6.4
$C_2O_4^{2-}$	0.27 ± 0.21	0.1 ± 0.04	0.13 ± 0.05
Formate	3.3 ± 2.8	1.7 ± 0.8	1.3 ± 0.6
MSA^-	0.94 ± 0.82	0.95 ± 0.83	0.51 ± 0.75
Na^+	48.4 ± 52.4	4.1 ± 6.4	4.1 ± 3.4
NH_4^+	0.97 ± 0.84	0.35 ± 0.33	0.28± 0.14
K^+	3.1 ± 3.3	0.16 ± 0.23	0.14 ± 0.12
Mg^{2+}	6.4 ± 4.9	0.59 ± 0.78	0.54 ± 0.39
Ca^{2+}	5.2 ± 4.1	1.4 ± 0.85	1.13 ± 0.55